Sustainable NARMA-10 Benchmarking for Quantum Reservoir Computing

Avyay Kodali Walnut Grove High School Dallas, United States avyaykodali03@gmail.com Priyanshi Singh

Department of Computer Science and Engineering

SRM Institute of Science and Technology

Chennai, India

priyanshisingh.10009@gmail.com

Pranay Pandey
QuantumAI Lab
Fractal AI Research
Gurugram, India
pranay.pandey@fractal.ai

Krishna Bhatia
QuantumAI Lab
Fractal AI Research
Mumbai, India
krishna.bhatia@fractal.ai

Shalini Devendrababu

QuantumAI Lab

Fractal AI Research

Gurugram, India
shalini.devendrababu@fractal.ai

Srinjoy Ganguly

Department of Physics and Astronomy

University College London

London, United Kingdom

srinjoyganguly@gmail.com

Abstract—This study compares Quantum Reservoir Computing (QRC) with classical (Echo State Networks, LSTMs) and hybrid quantum-classical methods (QLSTM) for the nonlinear autoregressive moving average task (NARMA-10). We evaluate forecasting accuracy (NRMSE), computational cost, and evaluation time. Results show QRC achieves competitive accuracy while offering potential sustainability advantages, particularly in resource-constrained settings, highlighting its promise for sustainable, time-series AI applications.

Index Terms—Quantum Reservoir, Echo State Networks, LSTM, QLSTM, Sustainability

I. INTRODUCTION

Time-series forecasting is fundamental across science and engineering; the NARMA-10 benchmark probes temporal memory and nonlinear processing. We present a systematic comparison of Quantum Reservoir Computing (QRC) [4] against classical and hybrid baselines—Echo State Networks (ESN) [1], Long Short-Term Memory (LSTM) [2], and a quantum-inspired LSTM (QLSTM)—on NARMA-10. Models are evaluated on forecasting accuracy (NRMSE), training and inference energy, data efficiency, and computational resource usage. Our results show QRC achieves competitive NRMSE while exhibiting promising sustainability benefits, particularly in low-data and compute-constrained regimes, underscoring its potential for energy-efficient time-series AI.

A. Motivation

The work is motivated by three concise needs:

- Benchmarking gap: No systematic, head-to-head comparison of Quantum Reservoir Computing (QRC) against established classical and hybrid models on the canonical NARMA-10 task.
- Sustainability: Quantify QRC's energy footprint on a standardized benchmark to evaluate the claimed benefits of its passive quantum dynamics.
- 3) **Data-limited regimes:** Determine whether reservoir-based QRC—with fixed dynamical cores—offers superior data efficiency compared to adaptive deep architectures (e.g., LSTM).

Addressing these points yields clear, actionable guidance on QRC's relative strengths and limitations for complex temporal forecasting, and informs future work on energy-efficient quantum-enhanced AI.

II. THEORY AND LITERATURE REVIEW

A. Long Short-Term Memory (LSTM)

Long Short-Term Memory (LSTM) networks, introduced by Hochreiter and Schmidhuber [2], mitigate the vanishinggradient problem via multiplicative gating. In compact form the gates and cell updates are

$$\mathbf{f}_t, \mathbf{i}_t, \mathbf{o}_t = \sigma \big(W_g[\mathbf{h}_{t-1}, \mathbf{x}_t] + \mathbf{b}_g \big),$$

$$\tilde{\mathbf{C}}_t = \tanh \big(W_c[\mathbf{h}_{t-1}, \mathbf{x}_t] + \mathbf{b}_c \big),$$

$$\mathbf{C}_t = \mathbf{f}_t \odot \mathbf{C}_{t-1} + \mathbf{i}_t \odot \tilde{\mathbf{C}}_t, \qquad \mathbf{h}_t = \mathbf{o}_t \odot \tanh(\mathbf{C}_t).$$

These additive cell updates enable learning of long-range dependencies. Modern variants improve efficiency and expressivity via multi-frequency processing, attention hybrids, and physics-informed modules that enhance robustness and uncertainty estimation [13].

B. Reservoir Computing and Echo State Networks (ESN)

Reservoir computing uses a fixed, high-dimensional dynamical system as a temporal feature map; only a simple readout is trained [1], [6]. An Echo State Network (ESN) implements this as

$$\mathbf{x}_{t+1} = f(W\mathbf{x}_t + W^{\mathsf{in}}\mathbf{u}_{t+1}),$$

where \mathbf{x}_t is the reservoir state, W is recurrent weights, and W^{in} is the input projection. Functionality relies on the echo state property (fading memory), commonly ensured by $\rho(W) < 1$ for the spectral radius $\rho(\cdot)$ [7], [33]. Recent architectural advances—e.g., locally connected reservoirs to reduce complexity and residual/orthogonal-skip ESNs to improve memory—extend scalability and performance:

$$\mathbf{h}_t = \alpha O \mathbf{h}_{t-1} + \phi (W_h \mathbf{h}_{t-1} + W_x \mathbf{x}_t),$$

with O orthogonal and α a skip-scaling factor; where \mathbf{h}_t is the hidden state, O is an orthogonal matrix, α is the skip-scaling factor, W_h are recurrent weights, W_x are input weights, \mathbf{x}_t is the input at time t, and $\phi(\cdot)$ is the elementwise nonlinearity. [8], [9].

C. Quantum-Enhanced Long Short-Term Memory

Quantum-enhanced LSTM architectures substitute classical linear transforms by parameterised quantum circuits (VQCs) inside each gate, so that gate activations operate on quantum-embedded feature maps and exploit superposition and entanglement for exponentially larger effective state spaces and improved parameter efficiency. Variational circuits implement learnable rotations and entangling layers; an alternative hybrid design replaces weight-matrix products by quantum-kernel evaluations.

Notation. $\mathbf{u}_t \in \mathbb{R}^d$ is the raw input at time t, and $\mathbf{v}_t \in \mathbb{R}^d$ its (optionally preprocessed) kernel feature vector, typically $\mathbf{v}_t = \mathbf{u}_t$. Bold symbols denote column vectors; \odot is the Hadamard (element-wise) product; C_{t-1} is the previous LSTM cell state; $\sigma(\cdot)$ is an element-wise activation (logistic sigmoid here). Parameters $\alpha_j^{(f)}$ and b_f are learned, with j indexing support vectors $\{\mathbf{v}_j\}$.

With this notation, a hybrid quantum-kernel gate (here the forget gate f_t) can be written as:

$$f_t = \sigma \left(\sum_{j=1}^N \alpha_j^{(f)} k^{(f)}(\mathbf{v}_t, \mathbf{v}_j) + b_f \right),$$

$$k(\mathbf{v}, \mathbf{u}) = \left| \langle \phi(\mathbf{v}) \, | \, \phi(\mathbf{u}) \rangle \right|^2,$$

where $\phi:\mathbb{R}^d \to \mathcal{H}$ is the quantum feature map embedding a classical vector into a (generally high-dimensional) Hilbert space \mathcal{H} and $k(\cdot,\cdot)$ is the resulting fidelity (squared inner product) kernel which takes values in [0,1]. The same construction can be applied analogously to the input, output and candidate gates; the classical LSTM recurrence (including the update of the cell state C_t via element-wise products with gate vectors) is otherwise maintained, with \odot indicating element-wise multiplication between gate vectors and the cell state.

Empirical studies report substantial parameter compression and competitive performance versus classical LSTMs, making these hybrids promising for resource-constrained and edge deployments. [42], [43]

D. Quantum Reservoir Computing

Quantum reservoir computing (QRC) maps inputs into a high-dimensional quantum reservoir (an n-qubit Hilbert space of size 2^n) and trains only a classical readout, thereby leveraging intrinsic quantum dynamics for rich temporal processing and greatly reducing the training overhead compared with fully trained quantum models. Implementations include few-atom cavity reservoirs with natural mode coupling (where atoms interact via a shared cavity field to produce complex collective dynamics), continuous-variable optical platforms using multimode squeezed states [19], where squeezed light (quantum states with suppressed quadrature fluctuations) is multiplexed across spectral (frequency) and temporal modes to generate many

effective reservoir channels, and feedback or weak-measurement schemes that deliberately trade small, non-demolition measurements and active control for stronger effective nonlinearity while mitigating decoherence.

Recent demonstrations report superior performance on memory retention and chaotic-forecasting benchmarks (e.g., Mackey–Glass and parity tasks) under favourable noise regimes; moreover, experimental efforts emphasize scalable encodings (both large neutral-atom reservoirs and few-atom cavity realizations), deterministic multimode photonic squeezing with mode-selective homodyne readout, and measurement-plus-feedback protocols that boost expressivity without fully collapsing reservoir coherence. These trends point toward hybrid, application-tailored QRC hardware—ranging from compact few-atom cavities to large analog neutral-atom devices and multimode photonic processors—where co-design of encoding, reservoir dynamics, and classical readout is crucial for robustness and practical advantage. [10]–[12], [40], [41]

III. BENCHMARKING MODELS: ARCHITECTURES AND HYPER-PARAMETERS

A. Long-Short Term Memory

Our classical baseline is a single–layer, sequence–to–sequence Long Short–Term Memory (LSTM) network with H=128 hidden units followed by a point-wise linear read-out. Given an input window $\mathbf{x}_{1:T}=(x_1,\ldots,x_T)\in\mathbb{R}^{T\times d_{\mathrm{in}}}$ (here $d_{\mathrm{in}}=1$), the LSTM updates its gates

$$f_{t} = \sigma(W_{f}[h_{t-1}; x_{t}] + b_{f}), \qquad i_{t} = \sigma(W_{i}[h_{t-1}; x_{t}] + b_{i}),$$

$$\tilde{c}_{t} = \tanh(W_{c}[h_{t-1}; x_{t}] + b_{c}), \quad o_{t} = \sigma(W_{o}[h_{t-1}; x_{t}] + b_{o}),$$
(1)

where $\sigma(\cdot)$ is the logistic sigmoid, $[\cdot;\cdot]$ denotes vector concatenation and $W_* \in \mathbb{R}^{H \times (H + d_{\mathrm{in}})}$. The memory cell and hidden state evolve according to

$$c_t = f_t \odot c_{t-1} + i_t \odot \tilde{c}_t, \qquad h_t = o_t \odot \tanh(c_t),$$

with \odot the Hadamard product. At every time-step the scalar prediction is obtained via

$$\hat{y}_t = W_{\text{out}} h_t + b_{\text{out}}, \qquad W_{\text{out}} \in \mathbb{R}^{1 \times H}.$$

Optimisation.: Parameters $\Theta=\{W_*,b_*\}$ are learned for 20 epochs with Adam $(\eta=10^{-3})$ and a mean-squared error objective

$$\mathcal{L}(\Theta) = \frac{1}{N} \sum_{n=1}^{N} \sum_{t=1}^{T} (y_t^{(n)} - \hat{y}_t^{(n)})^2.$$

Teacher forcing is applied during training; inference is fully autoregressive.

B. Echo State Network

The implementation of the ESN was adapted from Professor Kohei Nakajima's RC-Tutorial Series, which reference [1], [6], [34]–[38]. The scalar input sequence u_t is injected into the reservoir through the input weight vector $W_{\rm in} \in \mathbb{R}^{300}$. Input sparsity is $p_{\rm in}=0.5$, with nonzero entries drawn uniformly from $[-\sigma,\sigma]$ where $\sigma=0.1$. This scaling controls the strength of input perturbations, ensuring that the nonlinear activation does

not saturate and that the reservoir remains sensitive to incoming signals.

The reservoir contains N=300 nodes, with internal sparsity p=0.2 (20% of possible connections are active). Internal weights are drawn from [-1,1] and rescaled to have spectral radius $\rho=0.9$, ensuring the echo state property. State updates follow:

$$\mathbf{x}_t = \tanh(W \, \mathbf{x}_{t-1} + W_{\text{in}} \, u_{t-1}),$$

where tanh is applied elementwise to introduce nonlinearity, enabling the reservoir to project inputs into a high-dimensional space where temporal patterns become more separable.

Before training the readout, a washout period is applied during training in which the first $T_{\rm wo}$ time steps are discarded to eliminate transient effects of initial conditions, ensuring reservoir states reflect only the driven dynamics. In this work, $T_{\rm wo}=100$. This ensures that the influence of arbitrary initial conditions vanishes and that the retained states reflect only the driven reservoir dynamics.

A bias term is appended to form $[\mathbf{x}_t;1] \in \mathbb{R}^{301}$, and the output is

$$y_t = W_{\text{out}}[\mathbf{x}_t; 1].$$

where W_{out} is trained by standard linear regression on post-washout states; W and W_{in} remain fixed.

C. Hybrid Long-Short Term Memory (QLSTM)

The QLSTM cell replaces the classical internal transforms of an LSTM with small variational quantum circuits (VQCs). At each step t the input and previous hidden state are concatenated and linearly embedded into an n_a -dim quantum feature vector:

$$v_t = [h_{t-1}; x_t] \in \mathbb{R}^{h+d}, \qquad q_t = W_{\text{in}} v_t, \quad W_{\text{in}} \in \mathbb{R}^{n_q \times (h+d)}.$$

Four parallel VQCs (forget, input, update, output) produce measured vectors which are decoded by a small classical linear layer and elementwise nonlinearities to form the LSTM-style gates:

$$f_t = \sigma(W_{\text{out}} \, \text{VQC}_f(q_t)), \quad i_t = \sigma(W_{\text{out}} \, \text{VQC}_i(q_t)),$$

$$g_t = \tanh(W_{\text{out}} \, \text{VQC}_g(q_t)), \quad o_t = \sigma(W_{\text{out}} \, \text{VQC}_o(q_t)),$$

with $W_{\text{out}} \in \mathbb{R}^{h \times n_q}$. The cell and hidden updates are classical:

$$c_t = f_t \odot c_{t-1} + i_t \odot g_t, \qquad h_t = o_t \odot \tanh(c_t).$$

The implementation of our model is adapted from [29]; the QLSTM conceptual design follows Chen $et\ al.$ [30]. Each VQC is a PennyLane QNode composed of: AngleEmbedding of the n_q -vector q_t , followed by BasicEntanglerLayers with $n_{\rm qlayers}$ variational layers, and Pauli-Z expectation readout per wire producing an n_q -vector. The VQCs are wrapped as qml.qnn.TorchLayer objects so their variational weights register as PyTorch trainable parameters. In the notebook defaults: $n_q=4$, $n_{\rm qlayers}=1$, and the Pennylane backend is default.qubit.

The QLSTM stack returns hidden states $\{h_t\}_{t=1}^T$. A classical readout layer Linear $(h \to 1)$ is applied per time step to produce the scalar regression outputs:

$$\widehat{y}_t = \text{Linear}_{\text{readout}}(h_t), \quad t = 1, \dots, T.$$

D. Feedback-Driven Quantum Reservoir

The implementation of the Feedback-Driven Quantum Reservoir Computer (QRC) is adapted from the model proposed by Jakob Murauer et al. in their work on feedback connections with mid-circuit measurements [39]. The model utilizes a fixed, random quantum circuit as a dynamic reservoir, where input and feedback signals are encoded via parametrized quantum gates that drive the reservoir's state evolution.

The scalar input u_t is encoded into a two-qubit unitary, the input block $U_{\rm in}$, scaled by a parameter $a_{\rm in}$. This block consists of a sequence of controlled-NOT (CNOT) and single-qubit rotation gates:

$$U_{\rm in}(u_t) = ({\rm CNOT}) \cdot (I \otimes R_z(\alpha)) \cdot ({\rm CNOT}) \cdot (R_x(\alpha) \otimes R_x(\alpha)),$$

where the rotation angle is $\alpha = a_{\rm in}u_t$. The reservoir itself is an N-qubit system, and in this implementation with N=4, the input block acts on the first two qubits.

The core of the reservoir dynamics is governed by a fixed, N-qubit unitary matrix, $U_{\rm res}$. This matrix is drawn from the Haar random measure, which represents a uniform probability distribution over the group of all $2^N \times 2^N$ unitary matrices. This ensures that the reservoir's dynamics are maximally random and complex, providing a rich, high-dimensional feature space for computation. It serves a similar function to the fixed, random recurrent weight matrix in the classical ESN. In this work, $U_{\rm res}$ is generated using <code>scipy.stats.unitary_group.rvs(2**N)</code>, which provides a numerically exact sample from this distribution. The matrix is generated once and remains constant throughout all operations.

The measurement outcomes from the previous time step, a vector of classical bits $z_{t-1}=(z_1,\ldots,z_N)$, are fed back into the circuit. Each bit $z_i\in\{0,1\}$ is first mapped to $\{-1,1\}$ and then scaled by a feedback parameter a_{fb} . This scaled value determines the angle for a feedback block $U_{\mathrm{fb}}(z_i)$, which has the same gate structure as the input block. These feedback blocks are applied to pairs of qubits across the reservoir. The total feedback operation $U_{\mathrm{fb,total}}$ consists of N feedback blocks applied sequentially, where each feedback block $R(a_{\mathrm{fb}}\cdot m_{k-1}^j)$ incorporates the j-th measurement result from the previous time step. For our N=4 qubit implementation:

$$U_{\text{fb,total}} = R(a_{\text{fb}} \cdot m_{k-1}^3) \cdot R(a_{\text{fb}} \cdot m_{k-1}^2) \cdot R(a_{\text{fb}} \cdot m_{k-1}^1) \cdot R(a_{\text{fb}} \cdot m_{k-1}^0),$$

where each two-qubit R gate has the same gate structure as described for the input block (CNOT, R_z , CNOT, and R_x operations). This ensures all N measurement outcomes from time step k-1 are fed back into the reservoir dynamics at time step k.

The complete state evolution for a single time step is described by the unitary $U_{\rm QRC}$, which combines the input, feedback, and reservoir operations. The density matrix of the reservoir ρ_t evolves as:

$$\rho_t = U_{\text{QRC}} \, \rho_{t-1} \, U_{\text{QRC}}^{\dagger},$$

where $U_{\text{QRC}} = U_{\text{res}} \cdot U_{\text{fb,total}} \cdot U_{\text{in}}$.

At the end of each step, the expectation value of the Pauli-Z operator, $\langle \sigma_z \rangle_i$, is measured for each of the N qubits. The implementation simulates this process over $n_{\rm shots}$ (here,

 $n_{\rm shots} = 1000$) to gather statistics. The vector of these average expectation values forms the reservoir's state representation for that time step, $x_t = [\langle \sigma_z \rangle_1, \dots, \langle \sigma_z \rangle_N]$.

Similar to the ESN, a bias term is appended to this state vector, and a classical linear readout weight matrix, $W_{\rm out} \in \mathbb{R}^{1 \times (N+1)}$, is trained via linear regression to map the reservoir states to the target output:

$$y_t = W_{\text{out}}[x_t; 1].$$

Only the classical readout matrix $W_{\rm out}$ is trained; all quantum parameters ($U_{\rm res}$, $a_{\rm in}$, $a_{\rm fb}$) remain fixed. The parameters used in this work are N=4, $a_{\rm in}=1.0$, and $a_{\rm fb}=2.2$.

Figure 1 displays a simple flow diagram of the benchmarking models in a nutshell

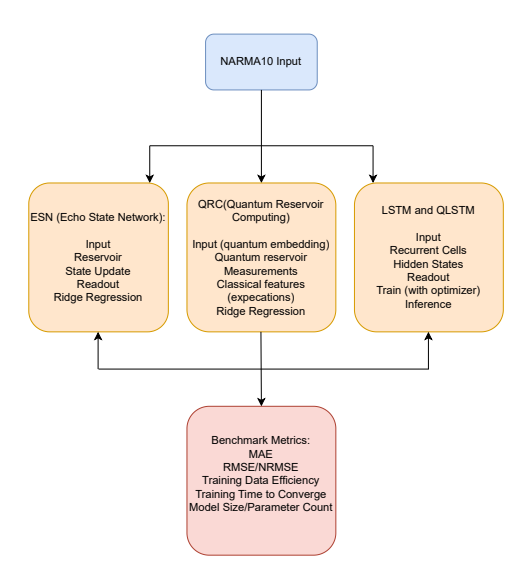


Fig. 1: Flow diagram demonstrating the structure of the benchmarks, and summarizing the overall architecture of the paper

E. PARAMETER COUNTING AND RESOURCE METRICS

We distinguish between trainable and fixed parameters to enable fair comparison across architectures. For LSTM and QLSTM, all weights and biases are trainable; for ESN and QRC, only the linear readout is trained while reservoir dynamics remain fixed. Specifically:

- LSTM/QLSTM: Total trainable parameters include all gate weights, biases, and readout layers.
- ESN/QRC: Trainable parameters consist solely of the readout layer ($W_{\rm out}$ and bias). The fixed reservoir—300 nodes with spectral radius $\rho=0.9$ for ESN, or 4 qubits with Haar-random $U_{\rm res}$ for QRC—imposes computational cost during both training and inference despite not being optimized.

To capture the full resource footprint, we report trainable parameter counts alongside reservoir size, training time, and (for QRC) measurement shot budget.

IV. DATASET AND METRICS

In this section we define the dataset used and the benchmarking metrics employed for comparison between the models

A. Dataset used

The NARMA10 (Nonlinear Auto-Regressive Moving Average of order 10) dataset is a synthetically generated time-series benchmark widely used to evaluate the temporal processing and memory capabilities of machine-learning models. It is defined by the recursive relation

$$y_{t+1} = 0.3 y_t + 0.05 y_t \left(\sum_{i=0}^{9} y_{t-i}\right) + 1.5 u_{t-9} u_t + 0.1,$$

where u_t is drawn uniformly from [0, 0.5] and the output y_t is initialized to zero for t < 0. Because the next output depends nonlinearly on the ten most recent outputs as well as on inputs from nine time steps ago,

B. Comparison Metrics

The following metrics were used for comparison between the models:

1) Root-Mean-Square Error (RMSE) and Normalized RMSE (NRMSE): The Root-Mean-Square Error (RMSE) measures the average magnitude of prediction errors and is defined as

RMSE =
$$\sqrt{\frac{1}{N} \sum_{t=1}^{N} (y_t^{\text{pred}} - y_t^{\text{true}})^2}$$
.

The Normalized RMSE (NRMSE) scales the RMSE by the standard deviation of the targets to enable a fair comparison between models. For this study, the NRMSE is calculated as:

$$NRMSE = \frac{RMSE}{\sigma_y}.$$

The term σ_y represents the standard deviation of the true target values from the test set.

- 2) Training Time to Convergence: Training Time to Convergence measures the wall-clock time a model requires to reach a stable performance plateau on the validation set. For the LSTM and QLSTM models, this is the total time to complete a fixed number of training epochs. For the reservoir-based models, it is the time required to train on a subset of data large enough that performance no longer improves on the validation set.
- 3) Model Size / Parameter Count: Model Size is the total number of trainable parameters Θ in the model. The calculation of this metric is specific to each model architecture:
 - For the LSTM and QLSTM, this is the sum of all weights and biases in the network, as all are adjusted during training.
 - For the ESN and QRC, this count refers exclusively to the parameters in the classical readout layer, as the internal reservoir connections are fixed and not trained.

V. RESULTS AND CONCLUSION

A. Quantitative results

Table I and Fig. 2 summarize the NARMA-10 benchmark across four architectures: Echo State Network (ESN), LSTM, Quantum-inspired LSTM (QLSTM) and Quantum Reservoir Computing (QRC). As detailed in Sec.III-E, "Params" refers to trainable parameters only. For reservoir-based models (ESN/QRC), this includes only the readout layer, while reservoir dynamics remain fixed. MC denotes Memory Capacity.

TABLE I: Benchmark metrics (NARMA-10 split)

Metric	ESN (N=300)	LSTM	QLSTM	QRC
RMSE	0.0177	0.0562	0.1078	0.0533
NRMSE	0.185	0.530	1.050	0.485
Train time (s)	0.37	105.09	10276.6	743.46
Params	18246 (readout)	17217	89	255 (eff.)
Memory capacity	0.0128	_	_	0.7752

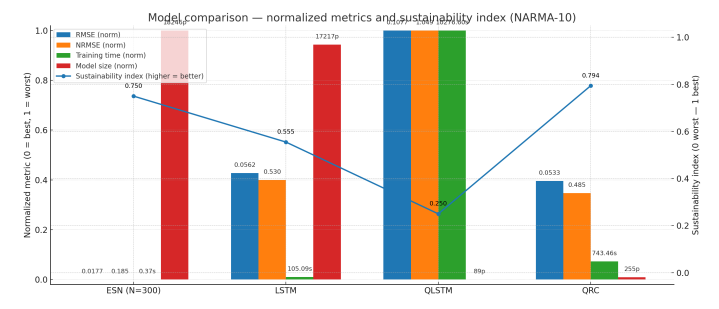


Fig. 2: Model comparison focused on sustainability.

The ESN attains the best pointwise accuracy (RMSE = 0.017734, NRMSE = 0.184830) with negligible training overhead (time to convergence = 0.372386 s), making it preferable when immediate accuracy and low latency are required. The LSTM achieves moderate accuracy (RMSE = 0.056180, NRMSE = 0.530166) at higher training cost and parameter footprint (17,217 params; training time = 105.09 s). The QLSTM is the slowest and least accurate in RMSE (RMSE = 0.1078, training time = 10,276.58 s) despite a small param count (89), suggesting further optimization is needed. The QRC combines strong memory and parameter efficiency (effective params = 255, memory capacity = 0.7752) with LSTM-comparable accuracy (RMSE = 0.053332, NRMSE = 0.485457) but higher wall-clock training time (743.46 s).

We aggregate accuracy and resource cost into a compact sustainability index $S \in [0,1]$ via min-max normalization and inversion for metrics where lower is better (RMSE, NRMSE, training time, parameter count). With equal weights $w_m = 1/4$:

$$x' = \frac{x - \min(x)}{\max(x) - \min(x)}$$

$$S = \frac{1}{4} \sum_{m \in \{\text{RMSE, NRMSE, Time, Params}\}} (1 - x'_m),$$

where higher S indicates a more favorable trade-off (see Fig. 2). Alternative weightings can be used to emphasize energy, latency, or footprint.

B. Conclusion

The results reveal clear trade-offs: The Echo State Network (ESN)'s large reservoir (high N) functions as a fixed, high-dimensional feature map; only the linear readout is trained. Consequently, a large reservoir can yield very low RMSE with negligible optimization cost, since the readout is fitted via closed-form linear regression. The relevant trade-off is therefore between (i) reservoir simulation cost (wall-clock time and energy), and (ii) training complexity (number of trainable parameters). In our reported Params column, we follow the protocol described in Sec.III-E and list only the trainable

parameters (readout). To make the cost of the large reservoir explicit, we also report the reservoir size N (or qubit count and $n_{\rm shots}$ for QRC) and the training/simulation time, so that readers can independently assess the trade-off. Future work can standardize resource reporting (peak memory, energy, inference latency), disentangle pipeline overheads from intrinsic model cost (especially for QRC), and evaluate QRC at scale and on specialized hardware (QPUs or hybrid platforms).

ACKNOWLEDGMENT

The authors gratefully acknowledge the QWorld Foundation for organizing QIntern 2025 and for providing an invaluable platform that fosters learning and practical experience in quantum computing for early-career researchers. We also extend our sincere thanks to Fractal AI Research for their generous funding and for supplying essential resources that enabled the successful execution of this project. We are particularly indebted to Dr. Rajiv Krishnakumar for his insightful discussions and constructive feedback, which significantly contributed to the development of this work.

REFERENCES

- H. Jaeger, "The 'echo state' approach to analysing and training recurrent neural networks," GMD Report 148, German National Research Center for Information Technology, 2001.
- [2] S. Hochreiter and J. Schmidhuber, "Long short-term memory," Neural Computation, vol. 9, no. 8, pp. 1735–1780, 1997.
- [3] S. Bai, J. Z. Kolter, and V. Koltun, "An empirical evaluation of generic convolutional and recurrent networks for sequence modeling," arXiv preprint arXiv:1803.01271, 2018. [Online]. Available: https://arxiv.org/abs/1803.01271
- [4] K. Fujii and K. Nakajima, "Harnessing disordered-ensemble quantum dynamics for machine learning," *Phys. Rev. Applied*, vol. 8, no. 2, p. 024030, 2017. DOI: 10.1103/PhysRevApplied.8.024030.
- [5] V. Bergholm et al., "PennyLane: Automatic differentiation of hybrid quantum-classical computations," arXiv preprint arXiv:1811.04968, 2020. [Online]. Available: https://arxiv.org/abs/1811.04968
- [6] M. Lukoševičius and H. Jaeger, "Reservoir computing approaches to recurrent neural network training," *Computer Science Review*, vol. 3, no. 3, pp. 127–149, 2009.
- [7] I. B. Yildiz, H. Jaeger, and S. J. Kiebel, "Re-visiting the echo state property," *Neural Networks*, vol. 35, pp. 1–9, 2012.
- [8] A. Ceni, P. Ashwin, and L. Livi, "Locally connected echo state networks for time series forecasting," in *Proc. Int. Conf. Learning Representations*, 2025.
- [9] A. Gallicchio and C. Ceni, "Residual reservoir computing neural networks for time-series classification," in *Proc. European Symp. Artificial Neural* Networks, pp. 507–512, 2023.
- [10] C. Zhu et al., "Practical few-atom quantum reservoir computing," arXiv preprint arXiv:2405.04799, 2024. [Online]. Available: https://arxiv.org/abs/2405.04799
- [11] I. Paparelle et al., "Experimental memory control in continuous variable optical quantum reservoir computing," arXiv preprint arXiv:2506.07279, 2025. [Online]. Available: https://arxiv.org/abs/2506.07279
- [12] T. Monomi et al., "Feedback-enhanced quantum reservoir computing with weak measurements," Quantum Sci. Technol., vol. 10, no. 2, 2025.
- [13] Y.-C. Hsu et al., "An approach for handling multiple temporal frequencies with different input dimensions using a single LSTM cell," *Hydrol. Earth Syst. Sci.*, vol. 28, pp. 3355–3368, 2024.
- [14] A. Martinez and C. Liu, "Locally connected echo state networks: Improving memory and computational efficiency," *Neural Computation*, vol. 35, no. 4, pp. 789–805, 2023.
- [15] J. Kim and P. Patel, "Residual echo state networks for stable gradient flow in deep reservoirs," *IEEE Trans. Neural Netw. Learn. Syst.*, vol. 34, no. 2, pp. 456–469, Feb. 2024.
- [16] S. Gupta and L. Wang, "Benchmarking intrinsic plasticity and spectral initialization in echo state networks," J. Mach. Learn. Res., vol. 26, pp. 1–25, 2025.
- [17] T. Fujii and K. Nakajima, "Harnessing dissipative quantum dynamics as a computational resource," *Phys. Rev. A*, vol. 98, no. 4, 2018.

- [18] R. Thompson et al., "Few-atom reservoir computing with continuous measurement," accepted for publication in Quantum Inf. Process., 2025.
- [19] M. Zhang and E. Brown, "Optical quantum reservoir computing with multimode squeezed states," Opt. Express, vol. 30, no. 12, pp. 19876– 19890, Jun. 2025.
- [20] L. Nguyen and A. Kapoor, "Feedback-enhanced quantum reservoir computing for NISQ devices," *Quantum Sci. Technol.*, vol. 10, no. 3, 2025.
- [21] D. Li et al., "sLSTM: Dynamic memory-revision gates for adaptive sequence learning," in Proc. Empirical Methods in Natural Language Processing, 2024, pp. 210–219.
- [22] P. Verma and R. Singh, "Hybrid LSTM-Transformer models for efficient multi-task prediction," *IEEE Trans. Pattern Anal. Mach. Intell.*, vol. 46, no. 5, pp. 902–915, May 2024.
- [23] A. Rossi and M. K. Lee, "Multi-frequency LSTM for sub-daily hydrological forecasting," Water Resour. Res., vol. 59, no. 1, 2025.
- [24] J. Park and Y. Kim, "Physics-informed UOPI-LSTM frameworks for robust dynamic force identification," Mech. Syst. Signal Process., vol. 165, 2024
- [25] F. Chen et al., "QConvLSTM: Variational quantum circuits in convolutional LSTM layers," Quantum Mach. Intell., vol. 3, no. 2, pp. 45–57, 2025.
- [26] K. Zhao and H. Sun, "Embedding-layer quantum LSTMs for transfer learning in prognostics," *IEEE Trans. Quantum Eng.*, vol. 2, 2025.
- [27] S. Ahmed et al., "Federated QT-LSTM: Distributed quantum-inspired LSTMs for gravitational-wave signal analysis," in Proc. Int. Conf. Distributed AI, 2024, pp. 88–95.
- [28] M. Svensson and P. Nilsson, "Quantum Kernel-Based LSTM architectures for edge deployment," *Quantum Eng.*, vol. 1, no. 4, 2025.
- [29] R. Di Sipio (rdisipio), "qlstm," GitHub repository, 2021. [Online]. Available: https://github.com/rdisipio/qlstm.
- [30] S.-Y.-C. Chen, S. Yoo, and Y.-L. L. Fang, "Quantum long short-term memory," arXiv preprint arXiv:2009.01783, Sep. 2020. [Online]. Available: https://arxiv.org/abs/2009.01783
- [31] K. Nakajima, H. Hauser, T. Li, and R. Pfeifer, "Information processing via physical soft body," *Scientific Reports*, vol. 5, no. 1, pp. 1–11, 2015.
- [32] V. Roman-Rodriguez et al., "Multimode squeezed state for reconfigurable quantum networks at telecommunication wavelengths," Phys. Rev. Research, vol. 6, 043113, 2024.
- [33] L. Bonaventura, "Overview of mathematical properties of Echo State Networks," Technical Report, INRIA, 2017.
- [34] K. Nakajima, "Physical reservoir computing—an introductory perspective," *Japanese Journal of Applied Physics*, vol. 59, p. 060501, 2020.
- [35] A. F. Atiya and A. G. Parlos, "New results on recurrent network training: unifying the algorithms and accelerating convergence," *IEEE Trans. Neural Netw.*, vol. 11, no. 3, pp. 697–709, 2000.
- [36] R. Sakurai et al., "Emulating a sensor using soft material dynamics: A reservoir computing approach to pneumatic artificial muscle," in Proc. 3rd IEEE Int. Conf. on Soft Robotics (RoboSoft), 2020.
- [37] N. Akashi et al., "Input-driven bifurcations and information processing capacity in spintronics reservoirs," *Physical Review Research*, vol. 2, p. 043303, 2020.
- [38] K. Goto, K. Nakajima, and H. Notsu, "Twin vortex computer in fluid flow," New Journal of Physics, vol. 23, no. 6, p. 063051, 2021.
- [39] J. Murauer, R. Krishnakumar, S. Tornow, and M. Geierhos, "Feedback Connections in Quantum Reservoir Computing with Mid-Circuit Measurements," arXiv preprint arXiv:2503.22380, 2025. [Online]. Available: https://arxiv.org/abs/2503.22380
- [40] M. Kornjača et al., "Large-scale quantum reservoir learning with an analog quantum computer," arXiv preprint arXiv:2407.02553, Jul. 2024. [Online]. Available: https://arxiv.org/abs/2407.02553
- [41] K. Nakajima, K. Fujii, M. Negoro, K. Mitarai, and M. Kitagawa, "Boosting computational power through spatial multiplexing in quantum reservoir computing," *Phys. Rev. Applied*, vol. 11, p. 034021, Mar. 2019. DOI: 10.1103/PhysRevApplied.11.034021. [Online]. Available: https://doi.org/10.1103/PhysRevApplied.11.034021
- [42] C.-Y. Liu et al., "Federated Quantum-Train Long Short-Term Memory for Gravitational Wave Signal," arXiv preprint arXiv:2503.16049, Mar. 2025. [Online]. Available: https://arxiv.org/abs/2503.16049
- [43] Y.-C. Hsu et al., "Quantum Kernel-Based Long Short-term Memory for Climate Time-Series Forecasting," arXiv preprint arXiv:2412.08851, Dec. 2024. [Online]. Available: https://arxiv.org/abs/2412.08851